Unterschrift BetreuerIn

TECHNISCHE UNIVERSITÄT WIEN
Vienna University of Technology

BACHELORARBEIT

Software implementation of the quality assurance tool for magnetic resonance imaging distortion assessment

ausgeführt am AKH

unter der Anleitung von

Professor

durch

David Blacher

Lindenbauergasse 7/29, 1110 Wien

April 18, 2017

Unterschrift StudentIn

Kurzzusammenfassung

deutsch?

Abstract

english

Contents

1 Introduction

1.1 Photon interaction

The intensity of light decreases as it travels through matter as described by Beer's law:

$$I(x) = I_0 e^{-\mu(h\nu, Z)x} \tag{1.1}$$

where x is the thickness of a homogeneous material and μ its linear attenuation coefficient, which is dependent on the energy of the photons ($h\nu$) and the proton number of the material (Z).

The reduction of intensity is due to a number of effects. The photons interact with electrons (photoelectric effect, Rayleigh scattering, Compton effect), with the electric field of the nuclei (pair production) or with the nuclei itself (photo nuclear reactions). The probability of those interactions differ for each material (Z) and photon energy ($h\nu$). This behaviour is implicitly considered in the attenuation coefficient $\mu(h\nu, Z)$.

For a photon being transmitted through matter with varying properties, the attenuation coefficient changes, too. After travelling a distance d, the intensity can be expressed as:

$$I(x) = I_0 e^{-\int_0^d \mu(x)dx} \tag{1.2}$$

Where $\mu(x)$ describes the attenuation at every distance x.
FIGURE WITH ATTENUATION COEFFICIENT

1.2 X-ray projection imaging

A widely used imaging technique based on the aforementioned photon interactions is X-ray projection. Its setup is made up by a light source, the object of interest, and a

receptor. Since the technique is about projection, a patient needs to be placed between an X-ray tube and the receptor (usually film-cassette or digital sensor). In the first stage of the imaging process, X-ray photons emitted by the tube enter the body. Next, while travelling through human tissue, they interact with its atoms in various ways (see 1.1). These processes govern how much light is absorbed or scattered. Finally, Photons which make it through the patient are recorded as they reach the receptor on the opposite side. This results in a negative greyscale image, where brightness values correspond to the intensity reduction. Low intensity (= high absorption) leads to bright spots on the image and vice-versa. The whole process could also be described as 'the projection of attenuation shadows on to the receptor', since the light absorption directly depends on the attenuation coefficient. The attenuation, on the other hand, depend on the tissue's properties (e.g. proton number Z, density, etc). Consequently, the attenuation shadows depict inner structures of the patient.

Soft tissue such as brain matter and muscles absorb only little light, casting a lighter shadow (dark areas on image) than bone which absorbs more photons (bright areas). Anything other than bone differs only slightly in attenuation, owing to the relatively small difference in atomic numbers and density. For this reason, X-ray projection imaging can be used to diagnose bone fractures, while at the same time it is not suited to clearly delineate soft tissue structures.

Other imaging modalities are better suited for the latter like medical ultrasound and Magnetic Resonance Imaging (MRI), to name a few. They are preferred for non invasive soft tissue examinations. If those imaging modalities are no option, X-ray projection can still be of some use in combination with contrast agents. Those substances fill the bloodstream with heavier atoms, which can be clearly seen against the dark background of surrounding soft-tissue. Studies of the gastrointestinal tract employ Barium compounds, for instance. Iodine is used as contrast agent for the circulatory system.

For patients allergic to those chemicals, a number of alternative agents have been developed. Unfortunately most introduce slight, sometimes serious side-effects. There is ongoing research to find materials yielding enhanced contrast while at the same time minimising adverse reactions, a promising candidate being gold nanoparticles.

2

1.3 Computer Tomography - CT

Computer Tomography (CT) is a three-dimensional (3-D) imaging modality based on the measurement of X-ray attenuation. The technique has evolved from 2-D X-ray scanning. By mounting source and receptor on a rotary ring with a patient at the centre, projections from any angle can be obtained. However, the receptor resembles an arc made up by 800 to 900 neighbouring detector elements instead of a 2-D array. A single image taken by the receptor is therefore only 1-D. Yet, by repeating this process from a sufficient number of different angles and along the entire patient (z-axis) a 3-D model can be computed. In contrast to 2-D methods, where the patients interior is projected/compressed onto a flat image, CT preserves the exact location information. This feature lead to a radical improvement in diagnostics.

Since its clinical introduction in 1971, CT has become a widely used 3-D imaging modality for a range of applications including radiation oncology. Especially in radiation therapy, knowledge of the exact geometry is crucial, which is why CT plays such an important role in treatment planning (see 1.4).

1.3.1 3-D image reconstruction

As a photon passes through the patient, it encounters different materials associated with characteristic linear attenuation coefficients. It is practical to think of the scanned body as a collection of $N = N_X \cdot N_Y \cdot N_Z$ finite size cubes (Δx cube length) called 'voxels' (analogous to pixels in a 2-D digital photograph). The entire model can then be regarded as a 3-D matrix, with the attenuation coefficients μ_i for all voxels as its entries. Figure 1.1 represents a $(4, 4, 1)$ matrix. It depicts the path an X-ray may follow passing through voxels with different values μ_i. This discretisation allows us to change equation 1.2 to:

$$I(x) = I_0 e^{-\sum_{i=1}^{N_X} \mu_i \Delta x} \tag{1.3}$$

The initial and final intensities can be read of the settings of the X-ray tube and the detected signal. Based on those values, image reconstruction algorithms derive the

three-dimensional linear attenuation coefficient matrix. For convenience the computed numbers are converted to Houndsfield Units, which are displayed in the final image.
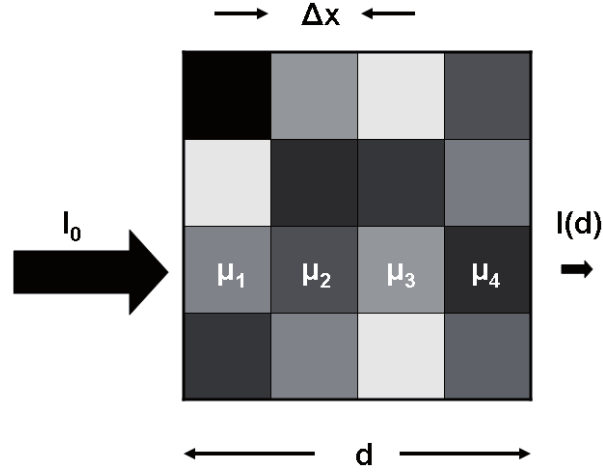

Figure 1.1: Simplified attenuation matrix (4,4,1)

1.3.2 Houndsfield Units

In a final CT scan voxel values are recorded in Houndsfield Units (HU), which relate to the attenuation of water at room temperature:

$$HU_{material} = \frac{\mu_{material} - \mu_{water}}{\mu_{water}} \cdot 1000 \tag{1.4}$$

Table 1.1 lists types of human tissue and their values on the HU scale. Generally HU values range from -1024 to +3071 (12 bit), but the upper limit can be extended to 15,359 (14 bit) if materials with even higher attenuation need to be visualised (e.g. implants).

Typically, CT scans are displayed on Computer monitors, which imposes the need to map the HU values to a 8-bit greyscale (256 steps of luminosity). Since the number of possible values (dynamic range) on the HU scale is 16 times the shades of grey on a screen (12-8 = 4 bit difference; equivalent to a factor of 2^4) the screen cannot convey all details at the same time. A linear mapping would result in 16 neighbouring values being compressed to the same brightness. This way, the brightest (bone) and darkest parts (soft tissue) of the image would be clearly distinguishable. At the same time small

Table 1.1: Average HU values for various types of human tissue

Substance	HU
Air	−1000
Lung	−750 (−950 to −600)
Fat	−90 (−100 to −80)
Water	0
Muscle	+25 (+10 to +40)
Brain, white matter	+25 (+20 to +30)
Kidneys	+30 (+20 to +40)
Brain, grey matter	+35 (+30 to +40)
Blood	+55 (+50 to +60)
Liver	+60 (+50 to +70)
Compact bone	+1000 (+300 to +2500)

differences (<16 HU) would appear as exactly the same intensity. Generally however, the doctor's focus might lie either on soft tissue or bone material. Bearing in mind that soft tissue values range only from 10 HU to 70 HU at most (see table 1.1), such a compression would make delineating organs using CT very unreliable. Instead of showing detail from the lowest to the highest value, a window of values can be chosen. Let's assume for example a range from -100 to 155 HU to be of interest. This selected range can be mapped directly and uncompressed to a 8-bit greyscale. Any values above 155 HU will be assigned the brightest value (white = 255), below -100 the darkest (black = 0). While showing very good soft tissue contrast, all bones would be depicted with exactly the same brightness (255), even though they might have a varying HU values. For bone structures a range from 300 to 2500 HU might show sufficient contrast. Standard computer programs used to display CT images allow the user to change the window interactively to any value range.

1.4 Types of External Beam Radiation Therapy

External Beam Radiation Therapy (EBRT) utilizes ionizing radiation to damage cancer cells in order to stop them from multiplying. This prevents the growth of tumours and eventually cures the patient. In conventional EBRT photons (x-rays) in the range of 4MeV to 20MeV are used to administer the necessary dose at the location of the tumour. Unfortunately, photons interact with all cells they're passing through until they are fully stopped. They release their energy slowly while travelling through the patient and usually get completely absorbed after leaving the body. Charged particles (e.g. protons, carbon ions) minimize the damage done to healthy tissue due to their distinctive behaviour in energy loss called "Bragg Peak". They release most of their energy shortly before stopping. [35] This effect can be used to spare tissue lying behind the tumour from radiation. [38] A comparison between x-rays and protons is shown in figure 1.2.
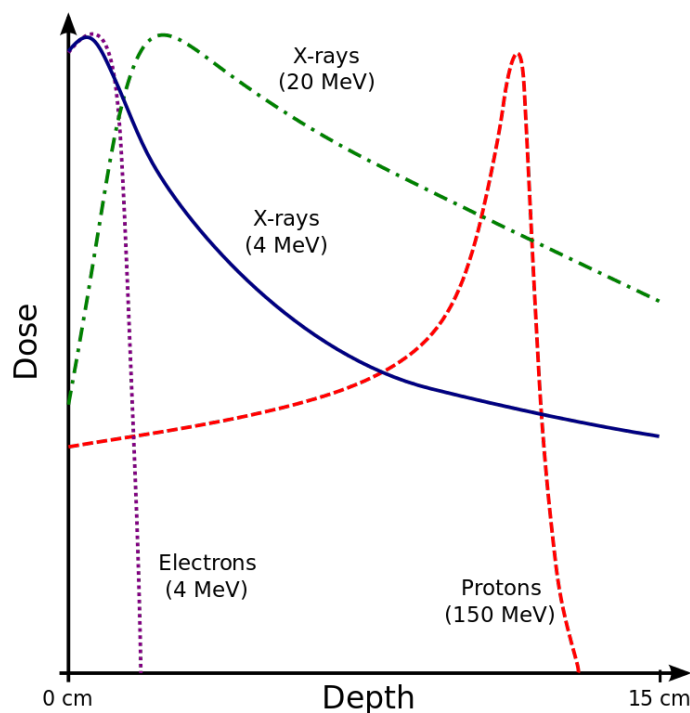

Figure 1.2: energy release of ionizing radiation
(By Cepheiden, via Wikimedia Common;
GFDL http://www.gnu.org/copyleft/fdl.html)

While travelling through matter both types of radiation release energy mostly due to coulomb interactions with the outer shell electrons of atoms. Knowing the electron density of of the targeted tissue area is therefore essential. In order to reach a specific penetration depth, the particles' initial energy has to be chosen accordingly.

1.5 Role of CT

Until recently radiotherapy treatment planning (RTTP) relied heavily on Computer Tomography (CT). There are two main reasons for this:

Firstly, CT uses low energy x-rays to create a 3D image of the patient. The luminosity value (brightness) assigned to each voxel (like pixel, but three-dimensional) corresponds to the local radiodensity recorded in Hounsfield units (HU). Materials with a higher radiodensity (e.g. bones) absorb more x-ray photons than those with less (e.g. water, brain-mater). Calculating the electron density using data obtained with CT is an easy task and used widely for RTTP. [9, 51] In order not to induce new cancer cells in healthy tissue during EBRT, the radiation beams are carefully targeted using the measured radiodensity. This way the absorbed dose accumulates in the cancer regions, while the nearby healthy tissue receives less radiation.

Secondly, CT images generate 3D images with little distortion. Exact geometries are needed for correct RTTP.

Image of RTTP

1.6 Role of MRI

Today RTTP often combines CT images with data acquired using Magnetic Resonance Imaging (MRI). MRI scans also record luminosity values, but they do not correspond to *HU* (radiodensity measured by CT). The signal intensity depends on many factors and even varies between MRI scanners.

MRI uses strong stationary magnetic fields to align magnetic spin moments of protons. Then an additional alternating field resonating with the spins is applied shortly to flip them 90°. Depending on the material spins then take longer or shorter to align again with the stationary field. Those differences can be measured in a pick-up coil surrounding the region of interest. The nature of this effect leads to a great contrast between soft tissue. [10] Delineating tumours using MRI images is more accurate than using CT. [46, 12, 47]

Another advantage of MRI over CT is the harmlessness of magnetic fields. CT utilizes the same type of radiation used for destroying cancer cells. Even though the radiation dose of a CT is low compared to radiation therapy, cancer patients need to be imaged frequently during treatment planning. Especially children treated with EBRT typically suffer from induced cancer occurring up to 40 years later. So while the benefit from using CT for diagnostics far outweighs the damage, there have been major efforts to reduce dose while maintaining reasonable image quality. [34, 5, 56, 55, 29, 16]

There are some difficulties arising from combining CT and MRI for EBRT: In order to profit from separately acquired data, the resulting images must be aligned either manually or automatically. This is a hard task since non-rigid objects (organs) change their shape and location between measurements. This leads to inaccuracies. Therefore MRI-only radiation therapy protocols are being developed: MRI data is used to create a Pseudo-CT, which contains information about electron density. Comparisons to using CT and MRI have shown acceptable deviations for X-ray therapy. In charged particle therapy the resulting dose gain in healthy tissue and dose loss in cancer regions due to inaccurately assigned electron density values is bigger. However, current development is promising. [45, 57, 36, 17, 7]

1.7 Open bore MRI scanners

The radiation oncology department of the Vienna General Hospital (AKH) is equipped with an 0.35T open-bore, c-arm MRI scanner. The open design improves the well-being of patients experiencing anxiety in closed scanners. Consequently, the number of incomplete MR examinations due to a claustrophobic events is low. [15, 3] Besides, patients who wouldn't fit in closed designed scanners can be imaged. Also, brachytherapy patients can be placed in the scanner with applicators attached.

This type of scanner is weaker than a conventional closed bore scanner (1-3 Tesla). High field strengths would result in greater resolution, better Signal to Noise (SNR) ratio, and faster imaging time. However, "There are definite cost advantages (capital, operating, siting) to the use of lower field MRI." [49] Permanent magnets are sufficient to create the 0.35T field. Therefore there is no need for constant cooling using liquid helium compared to superconducting magnets. Consequently, maintenance and service costs are considerably lower.

Generally, diagnostics benefit from greater image quality. However, at some point diagnostic accuracy stops increasing with field strength. Nevertheless, high field scanners are key to developing new methods such as functional MRI (fMRI) of the brain [14] and observing "metabolic reactions occurring in a human body in addition to producing very precise images of body structures" [60]. At the same time astonishing improvements can be achieved at low fields. A "combination of field independent polarization [...] with frequency optimized MRI detection coils [...] results in low-field MRI sensitivity approaching and even rivaling that of high-field MRI." [8]

One drawback of MRI, and especially open bore scanners, is the occuring distortion due to inhomogeneities in the magnetic field. For most applications small position shifts and deformations are of minor importance. In RTTP however, those effects can have a big impact. Therefore MRI scanners usually come equipped with an internal distortion correction algorithm. Those methods are developed by the company designing the scanners. Knowing the technical details enables them to drastically reduce the distortion.

Field of view (FOV) of the MRI scanner is smaller than the CT scanner's.

1.8 Aim of this work

The used open bore MRI scanner is not intended to be used for RTTP. The on board correction algorithm might not be good enough for effetive EBRT. The goal of this work is to commence the development of a quality assurance tool to asses the spatial distortion (after applying the internal correction). This is achieved by comparing MRI images to CT images used as a gold standard. An alerady existing custom designed phantom is provided by the AKH Vienna for this purpose. However, the liquid to fill the rods with has not been chosen yet. Therefore, this paper focuses mainly on the acquired data and which liquids to use the phantom with, not its entire design. However, possible fillings have to be produced and tested. Similar approaches are being used for distortion correction by other facilities. [42, 39, 58, 62, 63, 33]

2 Material and methods

2.1 Scanners

CT and MRI scanners used during this work are listed in Table 2.1.

System	product name	company	coil [internal W x H]
MRI	Magnetom C!	Siemens	Body/Spine Array Coil XL [50 x 30.5 cm (19.7 x 12 in)]
CT			——

Table 2.1: used scanners

2.2 Custom build phantom

To measure distortion the scanners must image a rigid object with known dimensions. Such phantoms are commercially available, but often expensive and designed for a specific calibration protocol. Some institutions build their own to fullfill exactly the requirements of a given application.

For the AKH it was important to create a lightweight phantom which can be imaged by CT and MRI scanners. Due to the underlying physics, only fluids are visible in MRI scans. CT however, also shows plastic. See figure 2.1 for a comparison (MRI/CT visibility). Therefore, they decided on plastic rods with a suitable fluid filling. Such a liquid should be easily produced, non-toxic, and yielding sufficient signal in MRI scans.

Commercially available phantoms often resemble water filled tanks containing plastic grids as a reference. This design results in stronger signal, but exceeds practical weight. There are few brands offering solutions utilising liquid fiducial markers in the shape of

pellets. They are arranged in a regular pattern surrounded by air or plastic. The AKH's design however relies on replaceable rods, which makes it a novelty.

(a) MR   (b) CT   (c) CT

Figure 2.1: Comparison: MRI only shows liquid filling, CT also the plastic rod and pane (horizontal black bar crossing middle and right rod);
(**a:**) *MRI* - filled rod, plastic not visible (field of view too small to show entire rod); (**b:**) *CT* - empty rod, plastic visible; (**c:**) *CT* - filled rod, plastic and filling visible

2.2.1 Frame and rods

For the open-bore MRI scanner the phantom was build to fit exactly the scanner's coil. Three parallel acrylic glass panes in the shape of the coil serve as a rigid frame. In the middle an empty area was reserved for an optional additional smaller phantom (not used for this work). Figure **??** shows an picture of the phantom. See also figure 2.2 showing a CT image of one pane (with no rods inserted).

More than 300 plastic rods (length: 50cm, outer diameter: 8mm, inner diameter: 4mm, volume: approx. 6mL) could be placed in the phantom. See figure 2.3 for a schematic sketch. The bottom part of each rod was sealed with a hot glued plastic plug, the top could be closed with a plastic screw. Frame and rods were already build and assembled before the author started working on this project.
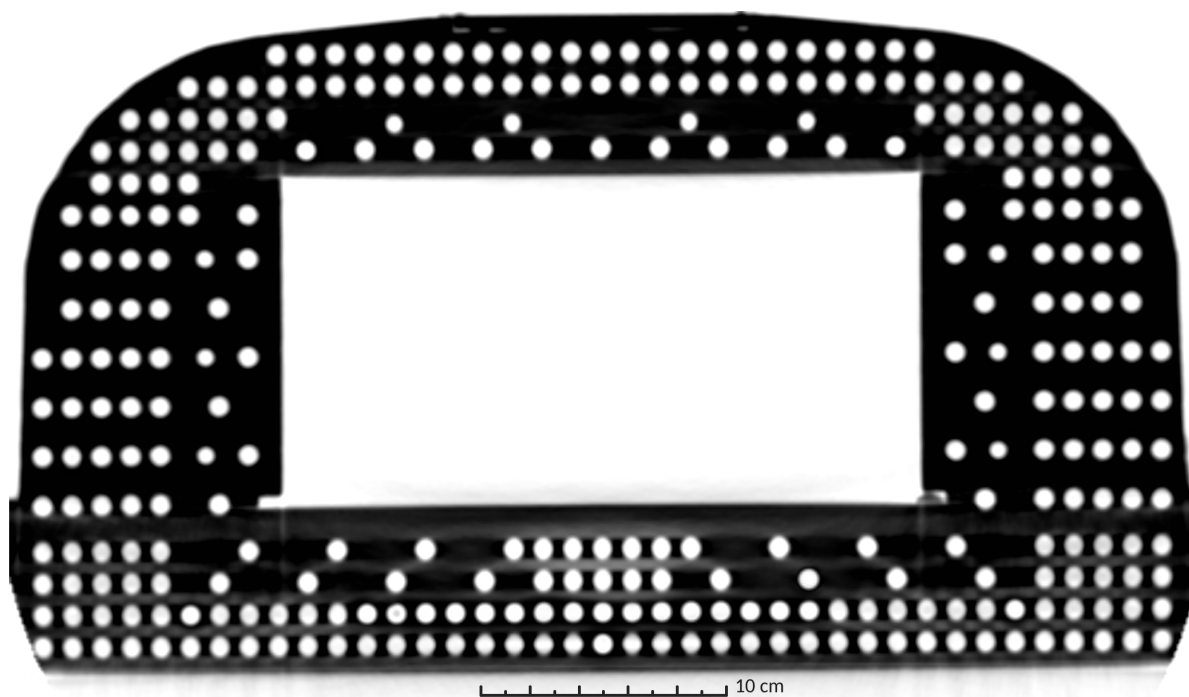
10 cm

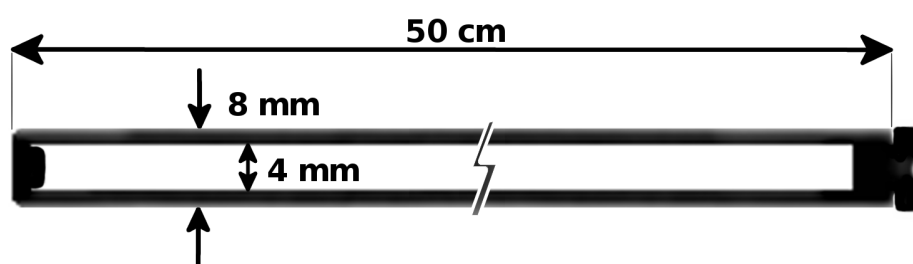Figure 2.2: plastic pane, no rods inserted

50 cm

8 mm

4 mm

Figure 2.3: empty plastic rod, schematic (not true proportions);

photo of Phantom   photo of single rod

2.2.2 Rod fillings

For this study 17 different liquids were produced to be tested as possible fillings. They are listed in Table 2.2.

Most tested fluids are based on water. This makes it easy to empty and clean the rods if needed. They could then be filled again with a different liquid. The chosen components are either non-toxic or harmless if not swallowed. Unfortunately the water might evaporate over time. To improve the mobility of trapped air bubbles, soap was added to some fluids.

As an alternative 2 oils were proposed. They do not contain water and air is not soluble in oil. Once a rod is completely with oil, no air bubbles should form. Using vegetable oil would be a non-toxic solution. This has been ruled out as a filling, because it would eventually rot. Mineral oil on the other hand does not rot.

Nr.	$NaCl$	$CuSO_4 \cdot 5H_2O$	Soap	Ascorbic Acid	Agar	Primovist [volume-%]
#1						
#2	3.6	1.96				
#3	3.6	3.92				
#4	3.6	19.6				
#5	3.6	1.96	1			
#6	3.6	1.96	5			
#7	3.6	1.96	20			
#8	3.6	1.96		0.36		
#9	3.6	1.96		3.6		
#10	3.6	1.96		36		
#11	3.6					0.1%
#12	3.6					1%
#13	3.6					10%
#14	3.6	1.96			0.5	
#15	3.6	1.96			20	
#16		Motor Oil:	*Castrol Power1*			
#17		Silicon Oil:	*Charge: 15HLVY023*			

Table 2.2: composition of tested solutions

(components in g/L; exception: Primovist in volume%)

#1 *destilled water* (as reference)

#2 $NaCl + CuSO_4 \cdot 5H_2O$ (as suggested by AAPM MR Subcommittee [21])

#3 increased concentration of $CuSO_4 \cdot 5H_2O$

#4 further increased concentration of $CuSO_4 \cdot 5H_2O$

#5 generic washing-up *soap* added to #2 (suggestion by Data Spectrum Corporation [11] to keep air bubbles from sticking to phantom walls)

#6 increased *soap* concentration

#7 further increased *soap* concentration

#8 *ascorbic acid* added to #2 (reduce forming of air bubbles by binding dissolved oxygen. It then degrades to dehydro-ascorbic acid and water. [2, 4] Concentration

of 0.36 g/L corresponds to approx. $0.00204\ mol/L$)

#9 increased *ascorbic acid* concentration

#10 further increased *ascorbic acid* concentration

#11 *Primovist* (a common contrast agent used for MRI scans [59, 48, 40])

#12 increased amount of *Primovist*

#13 further increased amount of *Primovist*

#14 *agar* (or agarose is commonly used as basic reference material for MRI phantoms [6, 28])

#15 increased *agar* concentration

#16 synthetic motor oil

#17 silicon Oil

Being closed at one end and having a capillary shape (small diameter) makes it impossible for the rods to be filled by pouring in the liquid. Instead of adding the fluid at the top, it has to be injected starting at the bottom. This way the contained air would pushed out through the opening on the top. A thin plastic tube was used to leave room for the gas to escape. Between different liquids the tube was flushed with #1 (distilled water) or #2 (main component of most solutions).

In order to minimize the amount of gas dissolved, the liquids were brought to boil shortly before injecting. Gas solubility generally decreases with rising temperature [19, 50] After injecting the solution in the rods, they were left to cool down. Before closing the rods were topped up completely (no trapped air bubbles). The oil based liquids, #16 and #17, were not brought to boil. Number #14 could be injected without problems, the solution remained fluid even after reaching room temperature. Number #15 on the other hand changed to a gel like consistence and clogged the tube right after the rod was filled. The tube could not be used again.

2.3 Sequences

Following the suggestions given in the Report of AAPM MR Subcommittee TG1 "MR Acceptance Testing and Quality Control" [21], T1 weighted sequences were chosen to evaluate the possible solutions. (Table 2.3)

System	—	—	—	—
MRI	-	-	-	-
CT	-	-	-	

Table 2.3: used sequences

2.4 Developed software tool

In order to asses the distortion of the MRI scanner, a tool was programmed. It is written in Python 2.7 and uses the *SimpleITK* package to read and process *DICOM* ("*Digital Imaging and Communications in Medicine*") files. [44, 13] *SimpleITK* is a object-oriented "C++ library with wrappers for Python, Java, CSharp, R, Tcl and Ruby". [52, 54] It's versatility is one of the reasons why this approach was favoured. It is a simplified layer built on top of the National Library of Medicine Insight Segmentation and Registration Toolkit (ITK). SimpleITK is also used by Applications like *3D Slicer* , a "free and open source software package for visualization and medical image computing". [1, 23] For this work 3D Slicer was used to crop images, quickly read values and visualize the results. Documentation and code examples of SimpleITK can be found at [53, 25] An alternative way to handle DICOM data in Python would be Pydicom. [43, 24]

An extensive list of packages used to process data:

- SimpleITK
- numpy
- scipy
- matplotlib.pyplot [20]
- skimage.draw
- datetime
- os

2.4.1 Processing MRI and CT scans

Prior to analising their data, the scans had to be prepared. To start with, they were aligned in a way that yields maximum overlap especially in the centre of the image. However, the MRI image had a lower resolution than the CT scan. Therefore, the MRI voxel's size were changed to match the CT voxels. Both images were resampled to CT

resolution. Those steps were performed using *MIRADA* (?????).

As described later, resolution might influence the efficiency of the distortion assesment. The application *3D Slicer* (Version: Slicer-4.5.0-1-linux-amd64) was used to again resample both images to a finer resolution.

Pixel spacing in x and y direction are equal. The z-axis, which lies approximately parallel to the phantom's rods, has a different pixel spacing. Overall image resolution could have a significant effect on the results. Therefore all calculations were made using original and interpolated (increased resolution) scans. See table 2.4 for more details. Figure 2.4 depicts 3 CT/MRI scans of a single rod (axial) with different resolutions. "x1" stands for the original CT scan resolution (MRI resampled to match). "x9" is a resolution resulting in 1 pixel being splitted in 9 smaller pixels, "x100" in 100, and so on. For better visibility images are printed with inverted colors. Dark pixels have a high density/intensity value, white pixels are equivalent to air (low density/intensity).

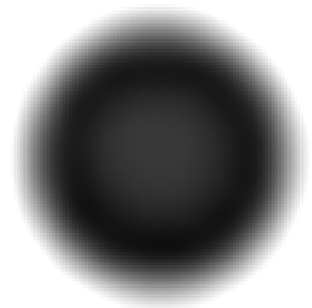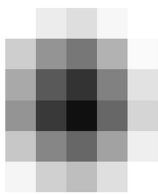| resample factor	z (not affected)	y (same as x)	x
x1	0.60	0.99	0.98
x4	0.60	0.49	0.49
x9	0.60	0.33	0.33
x25	0.60	0.2	0.2
x100	0.60	0.2	0.1

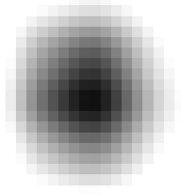Table 2.4: pixel Spacing (rounded values) [mm]
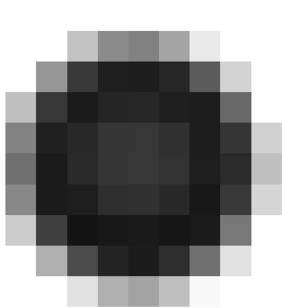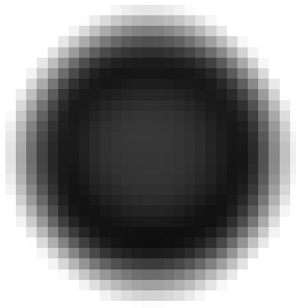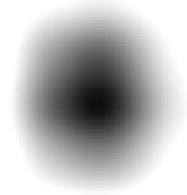
(a) CT x1 (b) CT x9 (c) CT x100

(d) MRI x1 (e) MRI x9 (f) MRI x100

Figure 2.4: CT/MRI: axial image of single rod, filling #5 (inverted colours)

2.4.2 Capabilities

The developed software tool is not able to automatically detect individual rods shown in a CT or MRI scan. Instead the acquired 3D images have to be cropped to depict only a single rod.

The python script can:

- denoise the image data
- find the brightness values of the rod, enabling it to
- separate pixels representing the rod from surrounding air (masking)
- calculate the centroid coordinates along the rod, used to
- calculate the local distortion

    loaction shift

    dice coefficient (roundness/deformation)

- plot individual rod slices

    overlaying one or two centroid coordinates

    and save it as ".png" file

- change the pixel values to reflect the distortion occuring along a rod (visualization)
- write the calculated numbers to a ".txt" file

2.4.3 Measuring distortion

Two phenomena were chosen to reflect the amount of distortion occurring in MRI scans:

1) location shift ("warp")

2) deformation (deviation from circular profile "DC")

Since the rods have a cylindrical shape, distortion can only be assessed in radial direction. To make calculations easier, the z-coordinate was put parallel to the rods, x and y radial. Each slice (z = const.) should idealy depict the bright circular profile of the liquid (+ plastic rod in CT) surrounded by black (air). To calculate the location shift between rods shown in CT and MRI, the coordinates of the center of mass (COM) were subtracted. The location difference in each slice is saved as an array. Additionally, the absolute value of the coordinate shift (absCS) could be calculated.

The dice-coefficient "DC" (also known as Sorensen-Index) was chosen as indicator for the deviation from a circular profile. Again this value was calculated for every slice using either the CT or MRI scans.

To get a idea of the occuring distortion one should look at both the absolute value of coordinate shift and the dice-coefficient (DC). The DC ranges from 0 to 1. A value of 1 indicates a perfect circular shape. A low DC on the other hand could be caused by many things such as: little overlap (e.g. a ring or crescent shape); a very dark image hindering delineation of rod from background; a small circle with a radius close to a only a few pixels.

2.4.4 Calculation: dice-coefficient (DC)

The dice coefficient or Sorensen index [32] is defined as:

$$DC = \frac{2|A \cap B|}{|A| + |B|} \tag{2.1}$$

The implementation into python is based on the open source python package "Medpy". [30] A part of it's module called "metric" was adapted. [31] All pixels above a certain threshold will be counted as input A. The reference B is a circle whose midpoint is placed at the COM.

The caluclation of the DC is done by comparing an binary image to a circle. The position of the circle's centre and its radius is highly influencing the outcome. Both the circle's centre and its radius were varied during the distortion assesment.

2.4.5 Calculation: center of mass (COM)

The calculation of the COM is done with help of the "scipy" python package. It's module "ndimage" contains the function "$center\_of\_mass()$", which returns the COM's coordinates of a given input array. The values assigned to voxels in CT images lie in the range from -1024 HU (air) to around 200 HU (plastic rod). Before a meaningful result can be obtained, the values need to be shifted to be > 0. Additionally, only pixels representing the rod or the liquid should be used for the calculation. Otherwise the almost black voxels surrounding the rod would influence the result. This error could be observed especially if the rod is not placed in the exact middle of the scan. As described earlier, the plastic rod is only visible in CT images. On the MRI scanns solely the liquid containded in the rods is shown. Therefore rods appear to be smaller on the MRI data. To find the relevant pixels two algorithms were developed:

1 calculating the number of pixels based on rod size

2 finding a COM resulting in good DC

add 1: The inner ($4mm$) and outer ($8mm$) diameter of the rods are known. So is the *pixel spacing* which respresents the equivalent size of a voxel in mm. Calculating the number of pixels which make up the more or less circular profile ot the rod in each slice is calculated like this:

$$pixelNumber = (radius^2 \cdot \pi) / (spacing^2) \qquad (2.2)$$

For CT images $radius = 4mm$, in MRI scans $radius = 2mm$. $spacing$ is the pixel spacing in x and y direction. Next the pixels are sorted by brigthness. The top $pixelNumber$ pixels are then used to calculate the COM.

add 2: This algorithm is a iteration method. It starts by assuming $\approx 50\%$ of all pixels in the image are part of the rod. This first guess of 50% is shifted by multiplying it with $(1 \pm 0.2) \rightarrow 1.2$ and 0.8. So in the first step two possible COMs are obtained using the brightest $50 * 1.2 = 60\%$ and $50 * 0.8 = 40\%$ of all pixels. It takes note of the values assigned to the darkest and brightest pixels used during both calculations. Those values are then set as threshold for the DC coefficient. Effectivly it finds COM and DC for 52% and 60%. If the DC for using 52% is bigger, it chooses $(100\% + 50\%)/2 = 75\%$ as next guess. If on the other hand the DC for 40% is bigger, it chooses $(0\% + 50\%)/2 = 25\%$ as next guess. In the second iteration it now again shifts the percentage by multiplying it with 1.2 and 0.8. Again COM and DC are calculated and the next guess is chosen by comparing the DCs. This is continued until the DC value decreases compared to DC found in prior steps. The maximum DC is used as indicator for the best COM.

3 Results

On the second day of working with the filled rods the one containing liquid #**6** broke (leakage). It happened when delicately knocking it against on the table while standing upright. This was intended to mobilise bubbles that sticked to the wall and make them travel vertically to on end of the rod. (see tabular 3.2) The plasic stopper on the lower end came loose. The rod containing filling #**6** was not replaced. Consequently, all CT and MRI images show only 16 rods.

3.1 Obtained MRI and CT scans

Figure 3.1 shows a coronal view of the 16 rods filled with the tested liquids. (in figure 3.2b a plasic bottle filled with water has been placed there instead (see figure 2.2).)
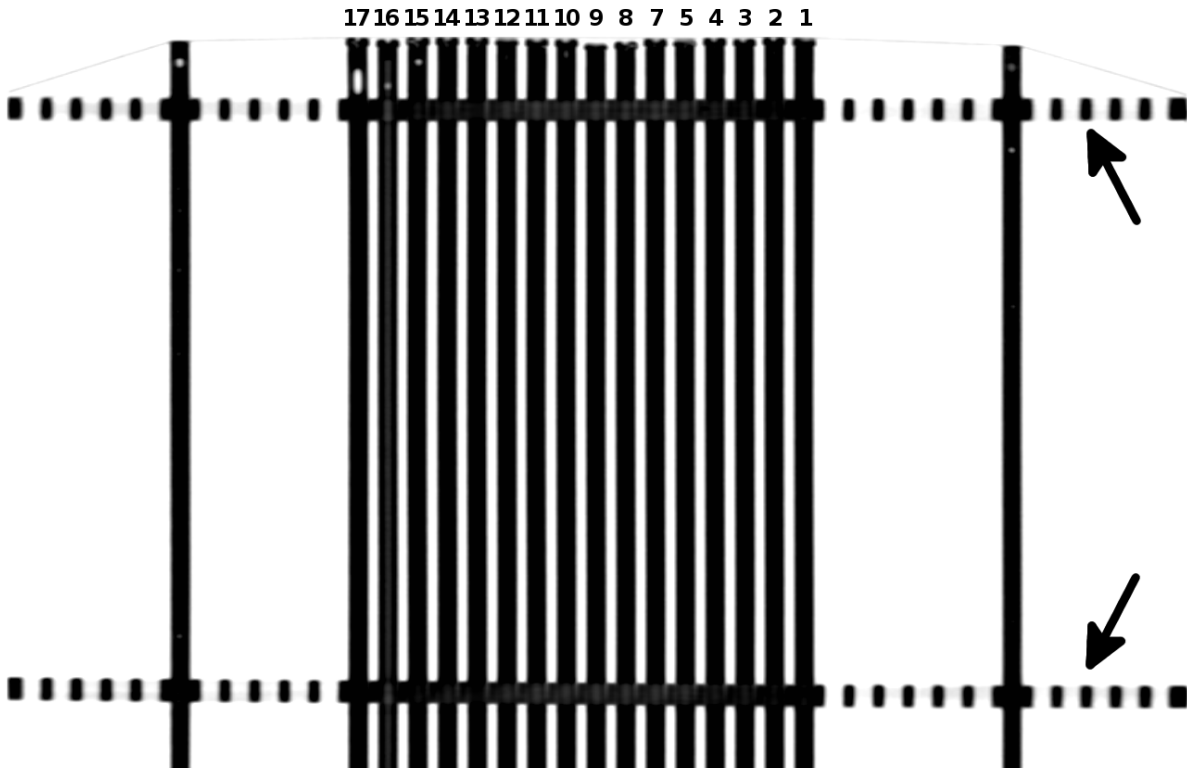
(a) CT: periodic black lines in upper and lower part of image (arrows) show plastic panes from above); rods have been fixed with adhesive tape (faint line across upper end of rods); differences in signal intensity (brightness) hardly noticeable, but air bubbles visible at upper end
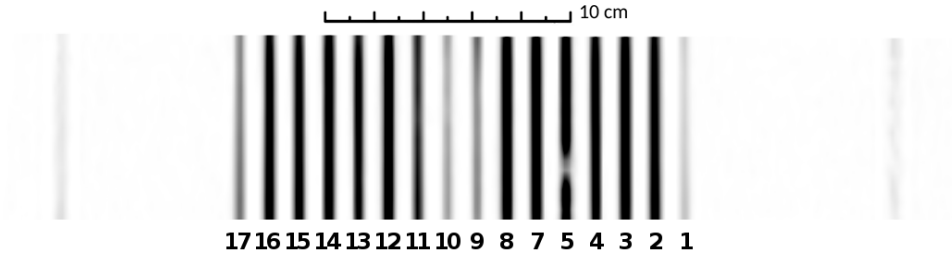

(b) MR: rods appear to be thinner, because only the liquid filling is visible; plastic (rods and panes) are not visible

Figure 3.1: Coronal CT/MRI (inverted colours; same scale; cropped images): images of 16 rods (tested liquids, numbering starting from the right, #6 excluded) + 2 reference rods (filled with water) on the sides; liquids result in different signal intensity (brightness)
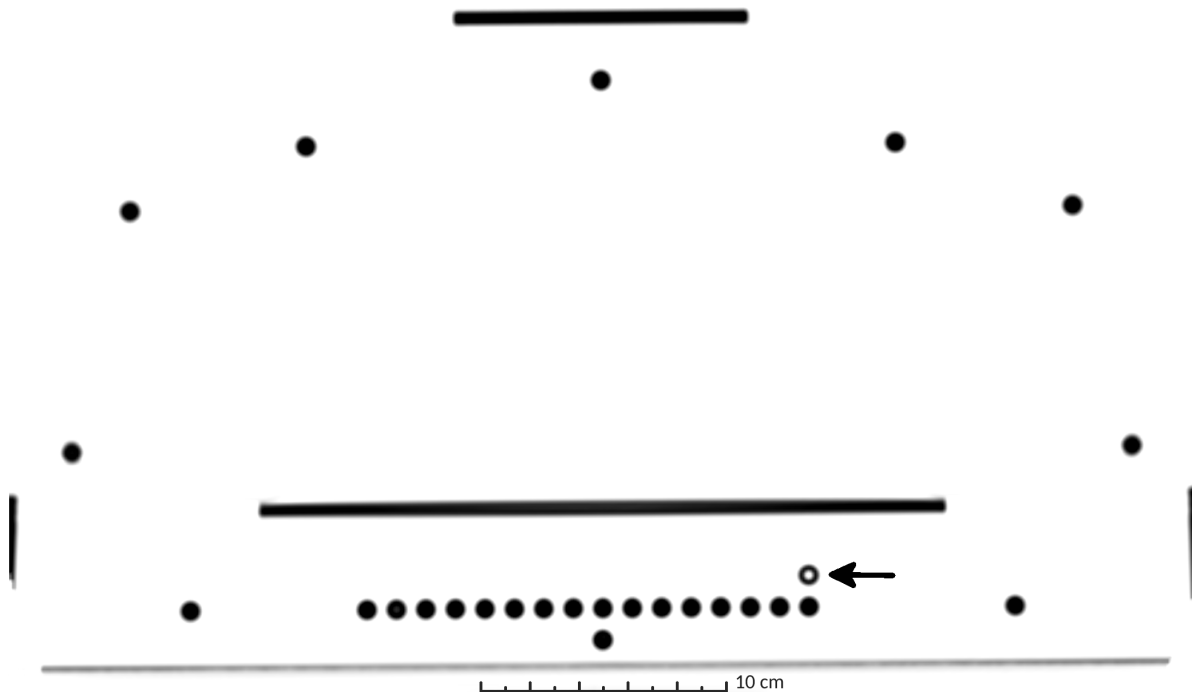
(a) CT: black bars just above tested rods, at the very top and to the sides show plastic parts of the phantom holding it togehter; faint grey line below tested rods shows table on which phantom was positioned during imaging
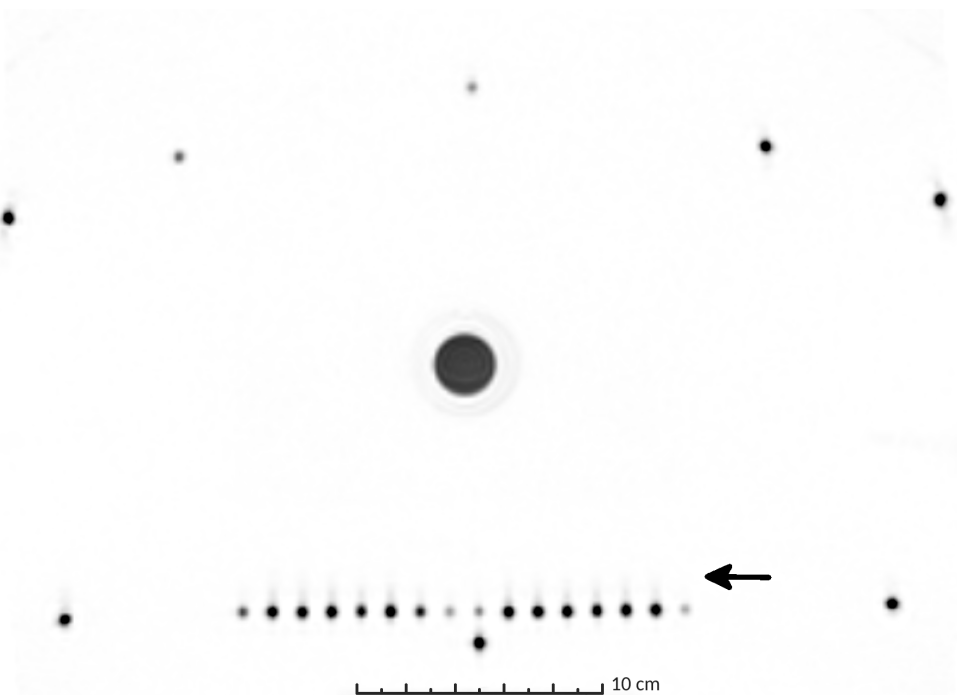
(b) MRI: black circle in middle shows water bottle which was placed in the middle of the phantom (necessary for MRI scanner to start imaging)

Figure 3.2: axial CT/MRI (inverted colours, same scale): images of 16 rods (tested liquids, numbering starting from the right, #6 excluded); surrounded by reference rods (filled with water) and one empty rod (marked with arrow) which is not visible on MRI scans

3.2 Tested solutions

3.2.1 Visibility on CT/MRI scans

Generally, imaging techniques aims for a high signal-to-noise ratio. Therefore, Liquids resulting in brighter pixels are favoured.

CT images show little differences between the tested liquids. The plasic rods themselves result in brigher pixels than any of the tested solutions.

On MRI scans most liquids had a mean and a max brightness value above 1000 (see table 3.1).

Only #1, #9, #10, & #17 resulted in significantly less signal.

3.2.2 Mechanical properties of solutions

A suitable filling would yield good image contrast in CT and MRI and acceptable mechanical properties.

The liquids were filled in a rod each and observed for several months. Some solutions produced air bubbles, which would eventually lead to incorrect calculations. Each rod was free of bubbles after sealing. The amount of gas inside the rods was measured after 2 months. Ideally, tilting the entire phantom slightly should be enough to fix all rods in the phantom at the same time. In some of the tested rods the produced air bubbles would stick to the wall. Only after gently hitting the rod they would start moving (see table 3.2).

Knowing the inner diameter d of the rods we can easily approximate the volume of gas trapped:

$$V = \frac{d^2}{4} \cdot \pi \cdot l \tag{3.1}$$

Nr.	Min	Max	Mean	Median	RMS	σ
1	182	371	288	269	296,3	69,8
2	1044	1921	1443,8	1405	1477,3	312,9
3	941	2075	1451,2	1394,5	1508,9	413,2
4	1176	1709	1440	1437,5	1458,6	232,5
5	1125	2111	1583,8	1549,5	1623	355
7	971	2241	1466,8	1316	1540,6	471,2
8	1459	1947	1704	1705	1713,5	180,5
9	385	584	486,8	489	495,6	93
10	247	502	343,6	266	361,1	111
11	830	1268	1036,2	1023,5	1049	163,2
12	1158	2211	1648,8	1613	1695,2	394,2
13	836	1657	1146,8	1047	1190,9	321,2
14	800	2062	1383	1335	1461,7	473,1
15	1156	1829	1476,2	1460	1501,2	272,7
16	1102	1967	1509	1483,5	1543,8	325,8
17	356	938	629,6	602	668,1	223,6

Table 3.1: liquid visibility on MRI scan

Nr.	after 1 day		after 2 days		after 1 week	
	bubbles	hit req.	bubbles	hit req.	bubbles	hit req.
#1	yes	no	no		no	
#2	yes	yes	no		no	
#3	yes	yes	no		no	
#4	yes	yes	no		no	
#5	yes	no	yes	no	no	
#6	yes	no	——— rod was leaking ———			
#7	yes	no	yes	no	yes	no
#8	no		no		no	
#9	no		no		no	
#10	no[1]		yes	yes	yes	yes
#11	no		yes,	*sticked to wall*	yes	yes
#12	yes	yes	yes,	*sticked to wall*	yes	yes
#13	yes	yes	yes,	*sticked to wall*	yes	yes
#14	no		yes	no	yes	yes
#15	no		no		no	
#16	no		no		no	
#17	no		no		no	

Nr.	after 2 months	
	lenght of trapped bubble l [mm]	approx. volume V [mm^3]
#1	2	25.13
#2	1.8	22.62
#3	1+1 (air blockage, at lower end)	25.13
#4	4	50.27
#5	1.5 (many small bubbles)	18.85
#6	——— rod was leaking ———	
#7	2 (many small bubbles)	25.13
#8	2.3	28.90
#9	3	37.70
#10	2.4	30.16
#11	2	25.13
#12	2	25.13
#13	2.3	28.90
#14	1.5+0.5 (big imobile bubble, at center)	25.13
#15	3.4 (agar gel dried)	42.73
#16	0	0.00
#17	0.5	6.28

28

3.3 Distortion assesment

All results were obtained by manually cropping the 3D image to depict only a single rod.

3.3.1 Distortion

table showing distrortion along z axis (isocentre to image border)

3.3.2 DC

(a) CT @ 0 (b) CT @ 150 (c) CT @ 304
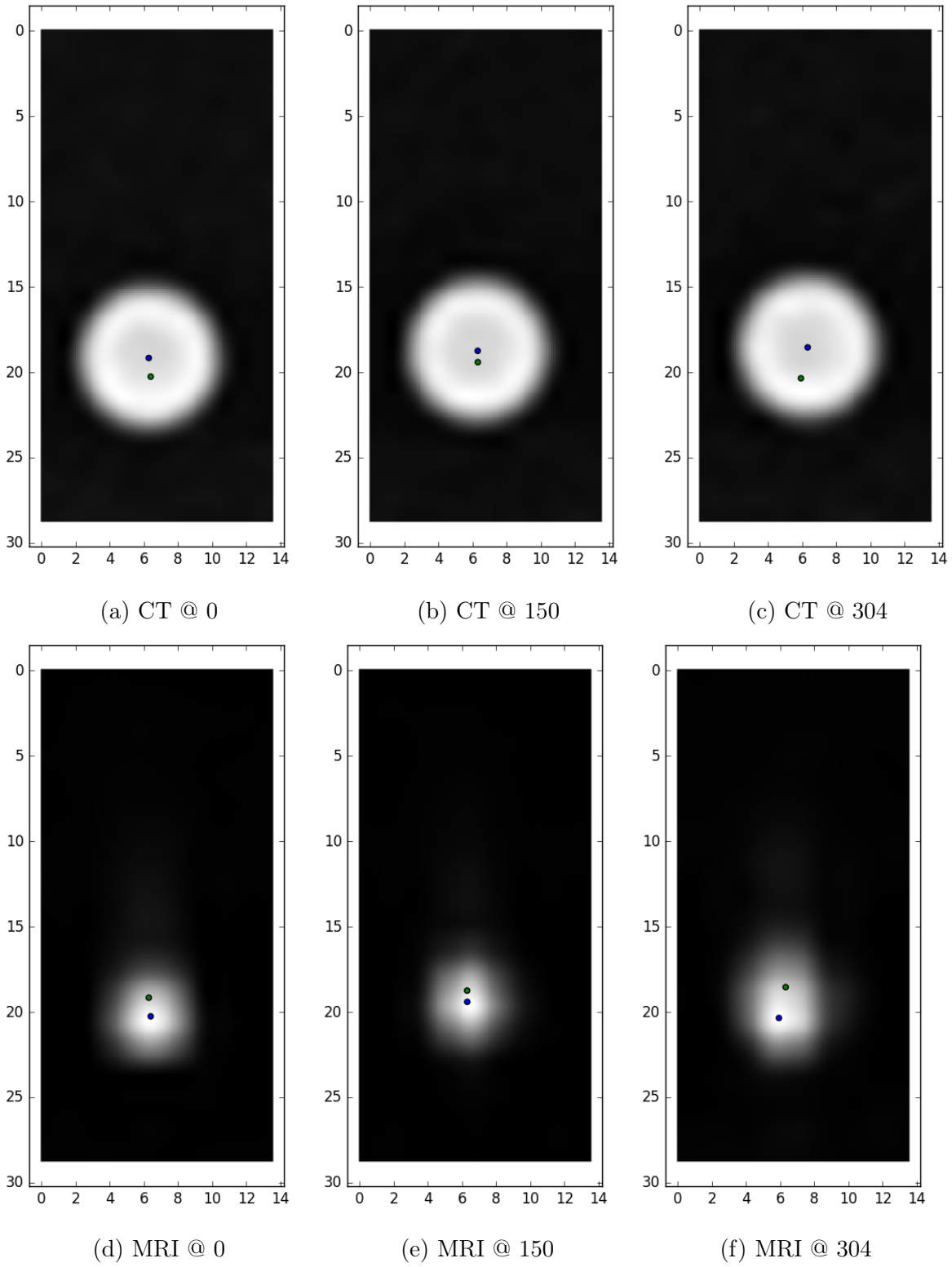
(d) MRI @ 0 (e) MRI @ 150 (f) MRI @ 304

Figure 3.3: MRI x100; blue dot centroid MRI, green dot centroid CT (same scale); slice 150 is approximately at the isocentre, 0 on the very end of the image, 304 close to an air bubble
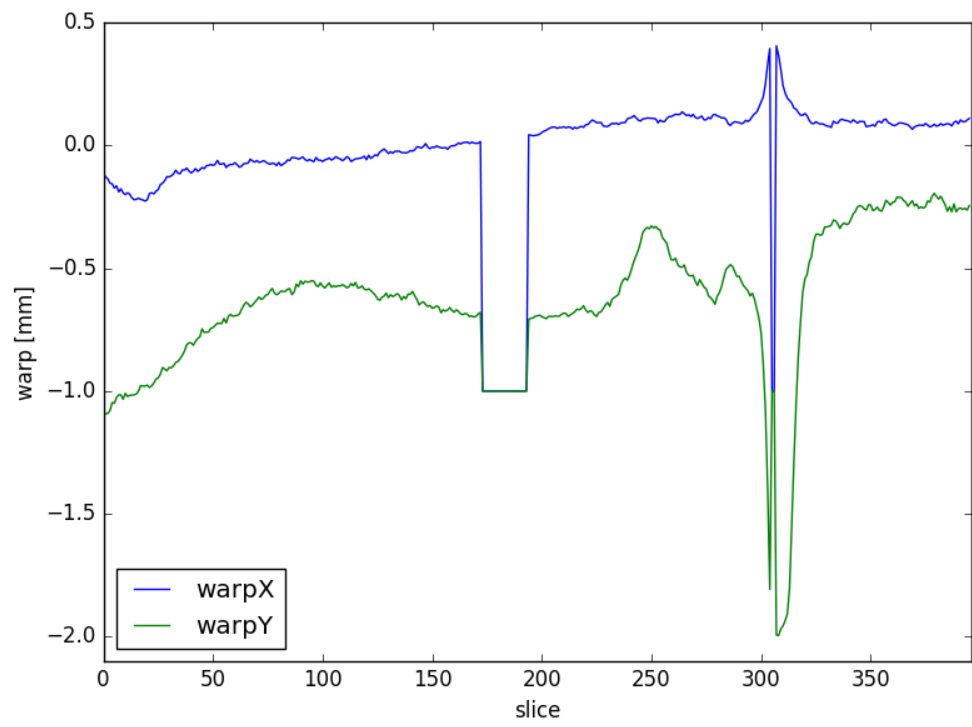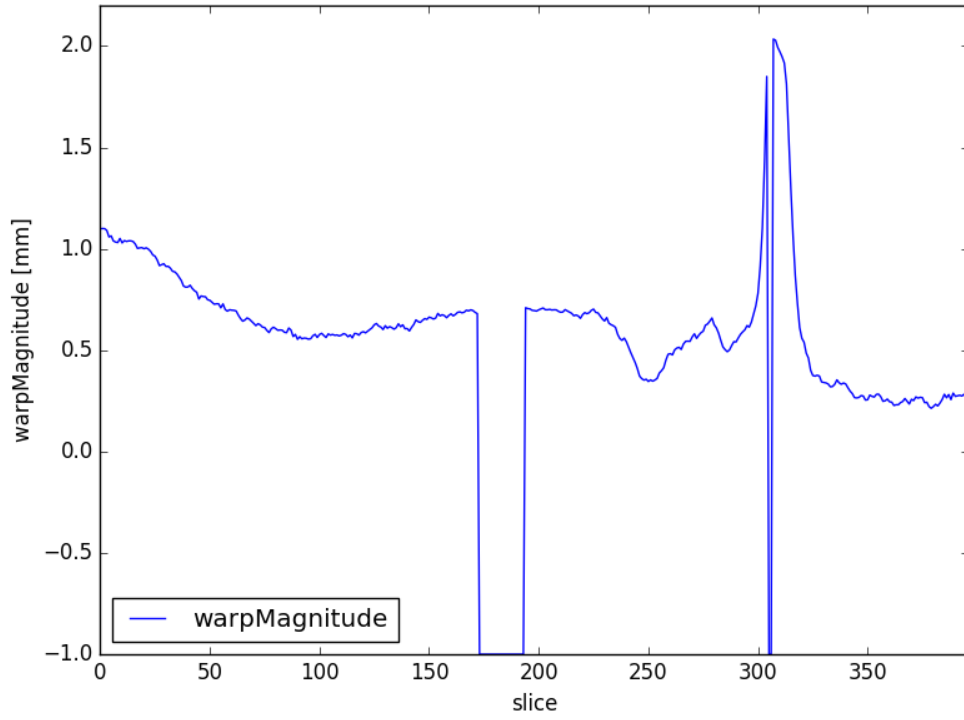
30

Figure 3.4: warp XY [mm], CT-MRI x100

Figure 3.5: warp Magnitude [mm], CT-MRI x100

The obtained dice coefficient varies not only because of the circle's centre and the radius, it also depends on the images resolution. Figure 3.8 and 3.9 show the DC (optimised) obtained using CT and MRI scans over resample rate.
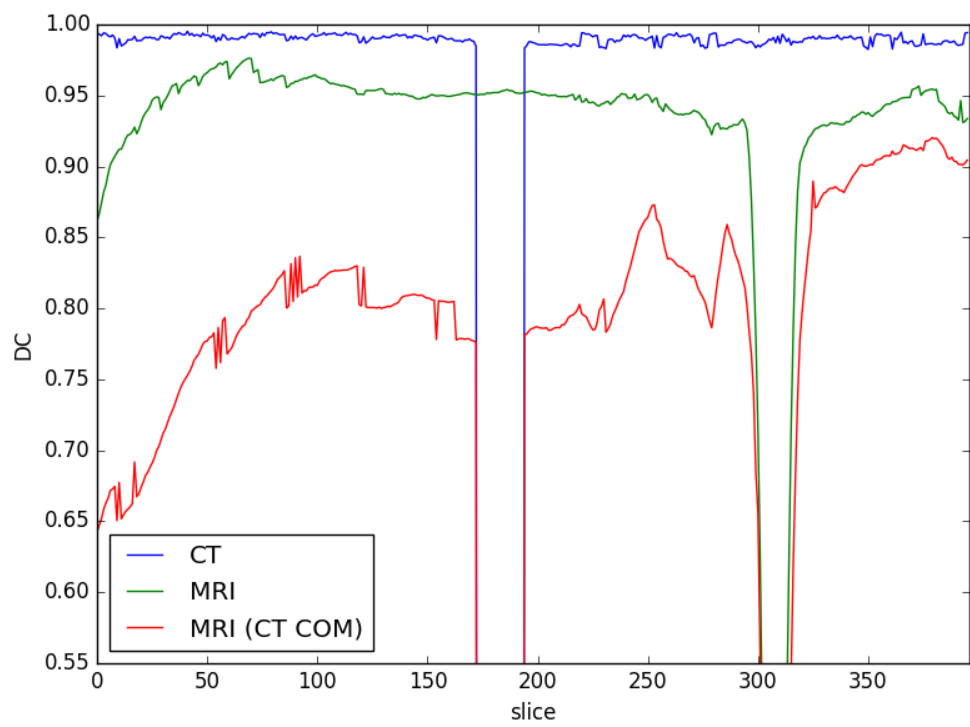
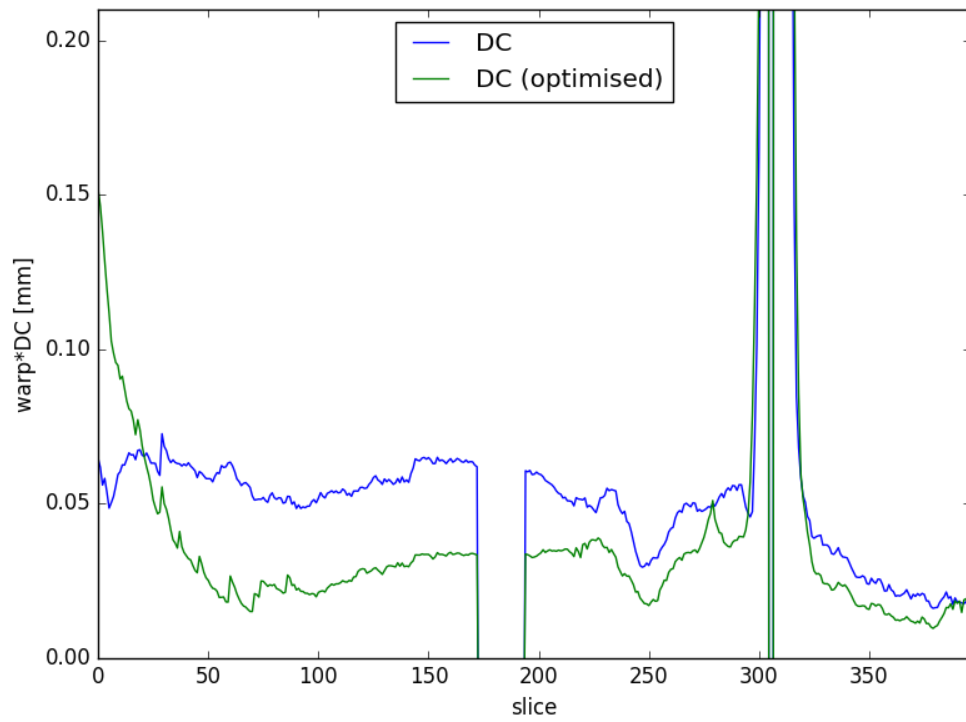Figure 3.6: DC (optimised) for CT & MRI & MRI (using CT COM)

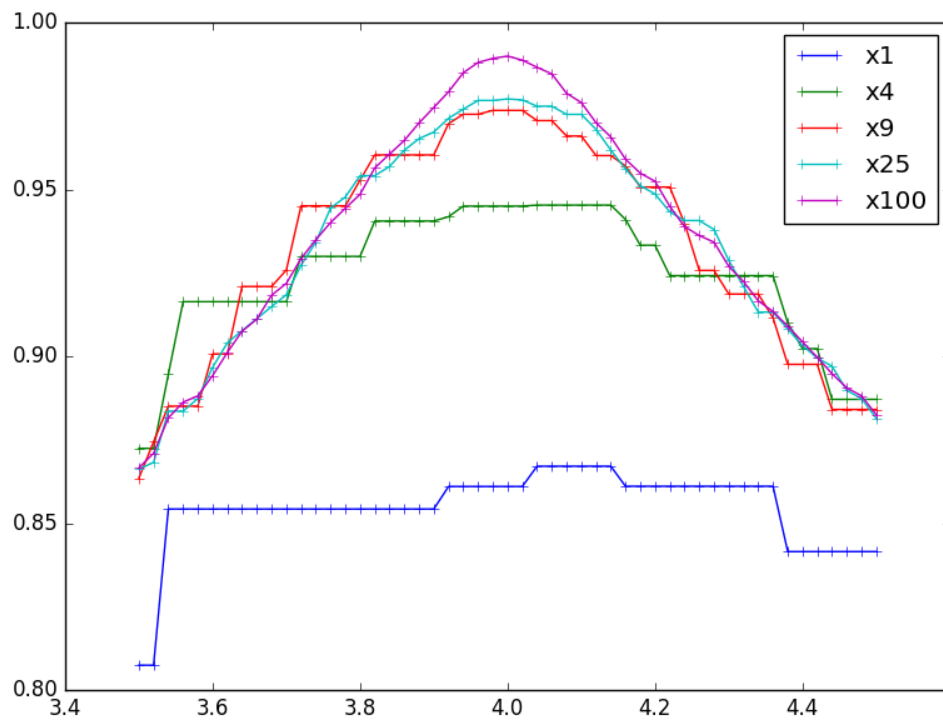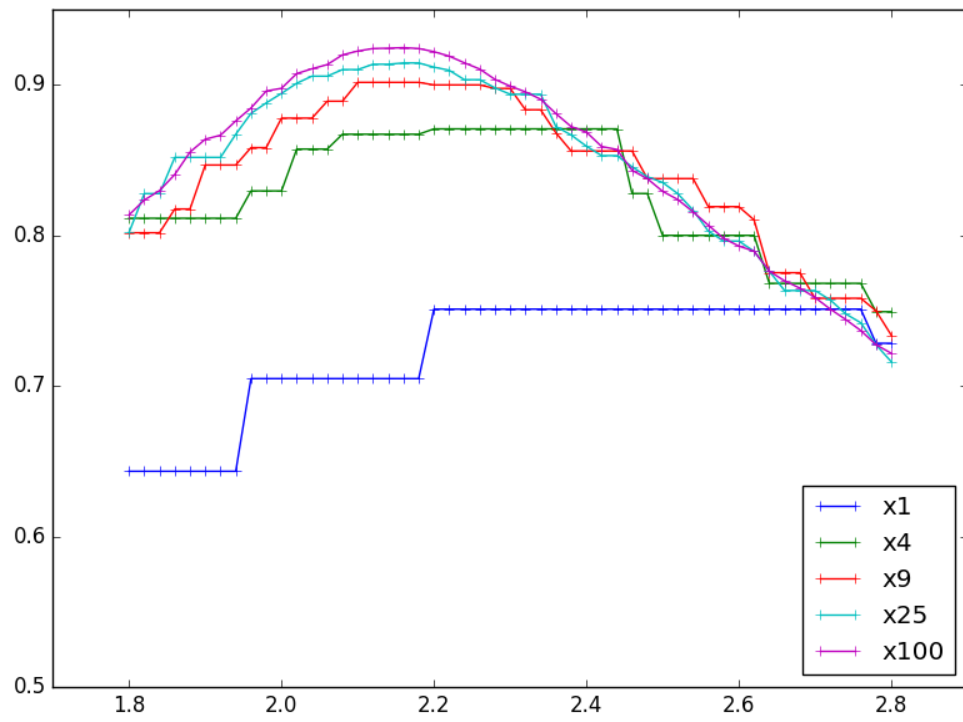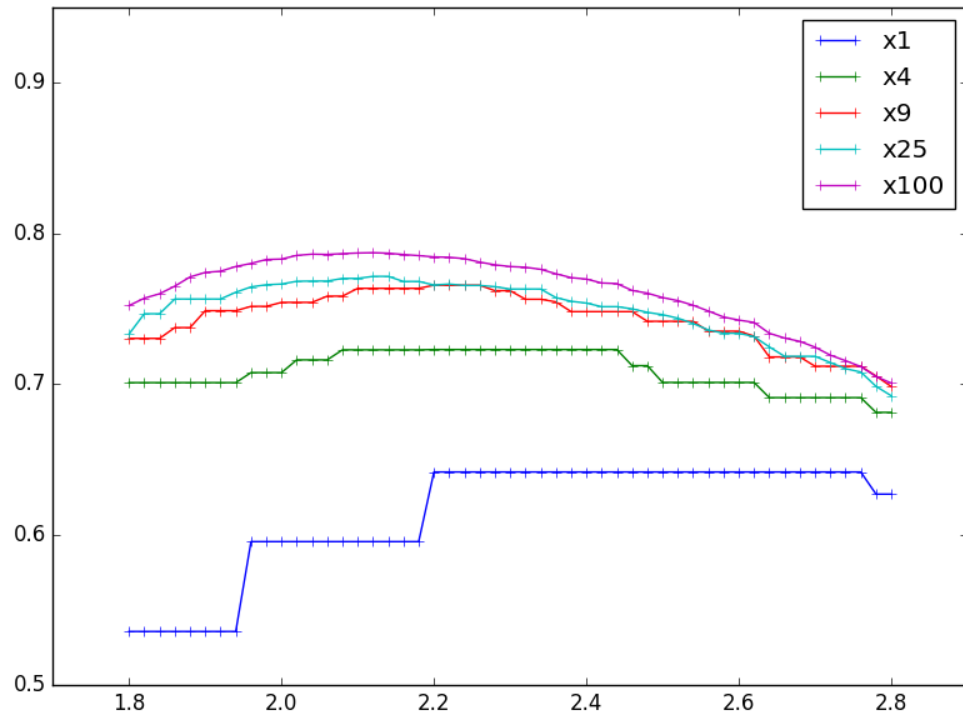Figure 3.7: artificial indicator warp*DC using real DC and optimised DC of MRI x100

Figure 3.8: CT: DC of varied radii & resolutions

(a) MRI: DC of varied radii & resolutions

(b) MRI: DC of varied radii & resolutions (using CT-COM)

Figure 3.9

4 Discussion

4.1 Tested solutions

For measuring the position of the rods in the CT scans the plastic rods without filling would be enough already, they would not be visible on the MRI scans, though.

Oil generally shows good visibility in CT and MRI scanns and produces no air bubbles after closing. However, filling all rods of the phantom with Oil is considered the last option. Water based liquids prove to be easier to clean. Since topping up over 300 rods regularily is too time consuming, oil seems to be a good alternative. However, if air bubbles could be easily shifted towards one end of the rod by tilting it slightly, they would lie outside the MRI scanner's field of view. Consequently, it would be sufficient to move air bubbles to one end of the rod before imaging.

4.2 Distortion

An air bubble might lead to a incorrect COM. Without looking at the dice-coefficient it's hard to tell why this distortion only appears to be present in a few slices. If both indicators show unexpected local irregularities, a conclusion might be easier to draw.

5 Conclusion and Outlook

5.1 Preparing the phantom for distortion assesment

5.2 Future improvement of software tool

Future improvements of the developed software tool are supposed to:

- find and register all individual rods automatically
- calculate the local distortion
- create a 3D vector map

Bibliography

[1] *3D Slicer.* \url{https://www.slicer.org/}.

[2] S. M. Abtahi, Majid Shahriari, M. H. Zahmatkesh, H. Khalafi, Sh Akhlaghpoor, and S. Bagheri. "A new approach to contrast enhancement in MAGICA gel dosimeter image with MRI technique". In: *Iranian Journal of Radiation Research* 6.3 (2008), pp. 151–156. ISSN: 17284562.

[3] Christopher Bangard, Jennifer Paszek, Frank Berg, Gesa Eyl, Josef Kessler, Klaus Lackner, and Axel Gossmann. "MR imaging of claustrophobic patients in an open 1.0 T scanner: Motion artifacts and patient acceptability compared with closed bore magnets". In: *European Journal of Radiology* 64.1 (2007), pp. 152–157. ISSN: 0720048X. DOI: `10.1016/j.ejrad.2007.02.012`.

[4] Richard S. Bodannes and Phillip C. Chan. "Ascorbic acid as a scavenger of singlet oxygen". In: *FEBS Letters* 105.2 (1979), pp. 195–196. ISSN: 00145793. DOI: `10.1016/0014-5793(79)80609-2`. URL: `http://doi.wiley.com/10.1016/0014-5793{\%}2879{\%}2980609-2`.

[5] D. J. Brenner, C. D. Elliston, E. J. Hall, and W. E. Berdon. "Estimated risks of radiation-induced fatal cancer from pediatric CT". In: *American Journal of Roentgenology* 176.2 (2001), pp. 289–296. ISSN: 0361803X. DOI: `10.2214/ajr.176.2.1760289`. arXiv: `01/1762âĂŞ289 [0361-803X]`.

[6] M L Bucciolini Ciraolo and B Lehmann. "SIMULATION OF BIOLOGIC TISSUES BY USING AGAR GELS AT MAGNETIC RESONANCE IMAGING". In: *Acta Radiologica* 30.6 (1989).

[7] Lili Chen, Robert A. Price, Lu Wang, Jinsheng Li, Lihong Qin, Shawn McNeeley, C. M Charlie Ma, Gary M. Freedman, and Alan Pollack. "MRI-based treatment planning for radiotherapy: Dosimetric verification for prostate IMRT". In: *Inter-*

national Journal of Radiation Oncology Biology Physics 60.2 (2004), pp. 636–647. ISSN: 03603016. DOI: 10.1016/j.ijrobp.2004.05.068.

[8]   Aaron M. Coffey, Milton L. Truong, and Eduard Y. Chekmenev. "Low-field MRI can be more sensitive than high-field MRI". In: Journal of Magnetic Resonance 237 (2013), pp. 169–174. ISSN: 10960856. DOI: 10.1016/j.jmr.2013.10.013. arXiv: NIHMS150003.

[9]   C Constantinou, J C Harrington, and L a DeWerd. "An electron density calibration phantom for CT-based treatment planning computers." In: Medical physics 19.2 (2012), pp. 325–327. ISSN: 00942405. DOI: 10.1118/1.596862.

[10]   Stuart Currie, Nigel Hoggard, Ian J Craven, Marios Hadjivassiliou, and Iain D Wilkinson. "Understanding MRI: basic MR physics for physicians." In: Postgraduate medical journal 89.1050 (2013), pp. 209–23. ISSN: 1469-0756. DOI: 10.1136/postgradmedj-2012-131342. URL: http://www.ncbi.nlm.nih.gov/pubmed/23223777.

[11]   Data Spectrum Corporation. Frequently Asked Questions - How do I eliminate air bubbles in the Mini, Micro and Ultra Micro line of phantoms? \url{http://www.spect.com/faq.html}.

[12]   Marc Debois, Raymond Oyen, Frederik Maes, Geert Verswijvel, Giovanna Gatti, Hilde Bosmans, Michel Feron, Erwin Bellon, Gerald Kutcher, Hein Van Poppel, and Luc Vanuytsel. "The contribution of magnetic resonance imaging to the three-dimensional treatment planning of localized prostate cancer". In: International Journal of Radiation Oncology Biology Physics 45.4 (1999), pp. 857–865. ISSN: 03603016. DOI: 10.1016/S0360-3016(99)00288-6. URL: http://www.sciencedirect.com/science/article/pii/S0360301699002886.

[13]   DICOM: About DICOM. \url{http://dicom.nema.org/Dicom/about-DICOM.html}. URL: http://dicom.nema.org/Dicom/about-DICOM.html (visited on 01/08/2017).

[14]   Jeff H. Duyn. The future of ultra-high field MRI and fMRI for study of the human brain. 2012. DOI: 10.1016/j.neuroimage.2011.10.065. arXiv: NIHMS150003.

[15]   Judith Enders, Elke Zimmermann, Matthias Rief, Peter Martus, Randolf Klingebiel, Patrick Asbach, Christian Klessen, Gerd Diederichs, Moritz Wagner, Ulf Teichgr??ber, Thomas Bengner, Bernd Hamm, and Marc Dewey. Reduction of claus-

trophobia with short-bore versus open magnetic resonance imaging: A randomized controlled trial. 2011. DOI: `10.1371/journal.pone.0023494`.

[16] Alice R. Goldman and Pierre D. Maldjian. *Reducing radiation dose in body CT: A practical approach to optimizing CT protocols.* 2013. DOI: `10.2214/AJR.12.10330`.

[17] Peter Greer, D Ph, Jason Dowling, D Ph, Peter Pichler, Jidi Sun, M Sc, Haylea Richardson, B Med Rad Sc, David Rivest-henault, D Ph, Soumya Ghose, D Ph, Jarad Martin, Chris Wratten, Jameen Arm, Leah Best, Jim Denham, and Peter Lau. "Development of MR-only Planning for Prostate Radiation Therapy Using Synthetic CT". In: (2015), pp. 61–62.

[18] Alexandra Hellerbach, Verena Schuster, Andreas Jansen, and Jens Sommer. "MRI Phantoms – Are There Alternatives to Agar?" In: *PLoS ONE* 8.8 (2013). DOI: `10.1371/`.

[19] William Henry. "Experiments on the Quantity of Gases Absorbed by Water, at Different Temperatures, and under Different Pressures". In: *Philosophical Transactions of the Royal Society of London* 93.1 (1803), pp. 29–274. ISSN: 02610523. DOI: `10.1098/rstl.1803.0004`. URL: `http://www.jstor.org/stable/107068?seq=1{\#}page{\_}scan{\_}tab{\_}contents`.

[20] J. D. Hunter. *Matplotlib: A 2D graphics environment.* \url{http://matplotlib.org/}. 2007. DOI: `10.1109/MCSE.2007.55`.

[21] Edward F Jackson. "MR Acceptance Testing and Quality Control : Previous MR Committee TG Reports MRI Acceptance Testing - E . Jackson Levels of Involvement MR Acceptance Test Reality Check MR Siting Issues". In: 17.1 (2009), pp. 287–295.

[22] Edward F. Jackson, Michael J. Bronskill, Dick J. Drost, Joseph Och, Wlad T. Sobol, and Geoffrey D. Clarke. *AAPM Report No. 100 Acceptance Testing and Quality Assurance Procedures for Magnetic Resonance Imaging Facilities Report of MR Subcommittee Task Group I.* 100. 2010, pp. 1–32. ISBN: 9781936366026.

[23] R Kikinis. *Overview: functions of 3D Slicer.* \url{http://perk.cs.queensu.ca/sites/perk.cs.quee 04-30-Kikinis-Slicer-reduced.pdf}. 2012.

[24]   Adamos Kyriakou. *DICOM in Python: Importing medical image data into NumPy with PyDICOM and VTK*. \url{https://pyscience.wordpress.com/2014/09/08/dicom-in-python-importing-medical-image-data-into-numpy-with-pydicom-and-vtk/}. (Visited on 01/10/2017).

[25]   Adamos Kyriakou. *Image Segmentation with Python and SimpleITK*. \url{https://pyscience.wordpre segmentation-with-python-and-simpleitk/}.

[26]   Tuong Le. "High-field, high-performance magnetic resonance: Technical challenges and clinical applications". In: *The journal of praktical medical imaging and mangement* (2004), pp. 1–8.

[27]   A.D.A Maidment and M.J Yaffe. "Mammography". In: *Diagnostic Radiology Physics A Handbook for Teachers and Students* (2014), pp. 209–235.

[28]   R Mathur-De Vre, R Grimee, F Parmentier, and J Binet. "The use of agar gel as a basic reference material for calibrating relaxation times and imaging parameters." In: *Magnetic resonance in medicine : official journal of the Society of Magnetic Resonance in Medicine / Society of Magnetic Resonance in Medicine* 2.2 (1985), pp. 176–179. ISSN: 0740-3194. DOI: `10.1002/mrm.1910020208`.

[29]   Cynthia H. McCollough, Andrew N. Primak, Natalie Braun, James Kofler, Lifeng Yu, and Jodie Christner. *Strategies for Reducing Radiation Dose in CT*. 2009. DOI: `10.1016/j.rcl.2008.10.006`.

[30]   *MedPy 0.2.2 : Python Package Index*. \url{https://pypi.python.org/pypi/MedPy}. URL: `https://pypi.python.org/pypi/MedPy` (visited on 12/19/2016).

[31]   *medpy.metric.binary — MedPy 0.2.2 documentation*. \url{http://pythonhosted.org/MedPy/_modul URL: `http://pythonhosted.org/MedPy/{\_}modules/medpy/metric/binary.html{\#}dc` (visited on 12/19/2016).

[32]   *medpy.metric.binary.dc — MedPy 0.2.2 documentation*. \url{http://pythonhosted.org/MedPy/gener URL: `http://pythonhosted.org/MedPy/generated/medpy.metric.binary.dc.html{\#}medpy.metric.binary.dc` (visited on 12/19/2016).

[33]   Takashi Mizowaki, Yasushi Nagata, Kaoru Okajima, Masaki Kokubo, Yoshiharu Negoro, Norio Araki, and Masahiro Hiraoka. "Reproducibility of geometric distortion in magnetic resonance imaging based on phantom studies". In: *Radiotherapy*

and Oncology 57.2 (2000), pp. 237–242. ISSN: 01678140. DOI: 10.1016/S0167-8140(00)00234-6.

[34] Martin J Murphy, James Balter, Stephen Balter, Jose a BenComo, Indra J Das, Steve B Jiang, C M Ma, Gustavo H Olivera, Raymond F Rodebaugh, Kenneth J Ruchala, Hiroki Shirato, and Fang-Fang Yin. "The management of imaging dose during image-guided radiotherapy: report of the AAPM Task Group 75." In: *Medical physics* 34.10 (2007), pp. 4041–4063. ISSN: 00942405. DOI: 10.1118/1.2775667.

[35] K Nakamura, E T Al., and (Particle Data Group). "Passage of particles through matter". In: *Journal of Physics* G.37 (2010), p. 075021. ISSN: 1434-6044. DOI: and2011partialupdateforthe2012edition.(pdg.lbl.gov).

[36] Tufve Nyholm and Joakim Jonsson. "Technical Aspects of MR-only Radiotherapy". In: (2015), pp. 65–67.

[37] Joseph G Och, Geoffrey D Clarke, Wladyslaw T Sobol, Coleman W Rosen Seong, Ki Mun, Coleman W Rosen, and Seong Ki Mun. "ACCEPTANCE TESTING OF MAGNETIC RESONANCE IMAGING SYSTEMS* Acceptance testing of magnetic resonance imaging systems: Report of AAPM Nuclear Magnetic Resonance Task Group No. 6 a)". In: *Reprinted from MEDICAL PHYSICS* 19.1 (1992), pp. 271–7344. ISSN: 0094-2405. DOI: 10.1118/1.596903.

[38] Harald Paganetti and Thomas Bortfeld. *Proton beam radiotherapy - The state of the art.* October. 2005, pp. 3–540. ISBN: 3540003215. DOI: 10.1118/1.1999671. URL: http://www.aapm.org/meetings/05AM/pdf/18-4016-65735-22.pdf.

[39] Bernhard Petersch, Joachim Bogner, Annette Fransson, Thomas Lorang, and Richard Pötter. "Effects of geometric distortion in 0.2 T MRI on radiotherapy treatment planning of prostate cancer". In: *Radiotherapy and Oncology* 71.1 (2004), pp. 55–64. ISSN: 01678140. DOI: 10.1016/j.radonc.2003.12.012.

[40] "Physico-Chemical Properties". In: ().

[41] E B Podgorsak. "Radiation Oncology". In: *Radiation Oncology* ().

[42] Ryan G. Price, Mo Kadbi, Joshua Kim, James Balter, Indrin J. Chetty, and Carri K. Glide-Hurst. "Technical Note: Characterization and correction of gradient non-linearity induced distortion on a 1.0 T open bore MR-SIM". In: *Medical Physics* 42.10 (2015), pp. 5955–5960. ISSN: 0094-2405. DOI: 10.1118/1.4930245. URL: http://scitation.aip.org/content/aapm/journal/medphys/42/10/10.1118/1.4930245.

[43] *Pydicom.* \url{http://pydicom.readthedocs.io/en/stable/getting_started.html}. (Visited on 01/10/2017).

[44] *Python 2.7.13.* \url{https://www.python.org/}. (Visited on 01/10/2017).

[45] Christopher M. Rank, Nora Hünemohr, Armin M. Nagel, Matthias C. Röthke, Oliver Jäkel, and Steffen Greilich. "MRI-based simulation of treatment plans for ion radiotherapy in the brain region". In: *Radiotherapy and Oncology* 109.3 (2013), pp. 414–418. ISSN: 01678140. DOI: 10.1016/j.radonc.2013.10.034.

[46] Coen Rasch, Isabelle Barillot, Peter Remeijer, Adriaan Touw, Marcel Van Herk, and Joos V. Lebesque. "Definition of the prostate in CT and MRI: A multi-observer study". In: *International Journal of Radiation Oncology Biology Physics* 43.1 (1999), pp. 57–66. ISSN: 03603016. DOI: 10.1016/S0360-3016(98)00351-4.

[47] Mack Roach, Pamela Faillace-Akazawa, Christine Malfatti, John Holland, and Hedvig Hricak. "Prostate volumes defined by magnetic resonance imaging and computerized tomographic scans for three-dimensional conformal radiotherapy". In: *International Journal of Radiation Oncology Biology Physics* 35.5 (1996), pp. 1011–1018. ISSN: 03603016. DOI: 10.1016/0360-3016(96)00232-5.

[48] Martin Rohrer, Hans Bauer, Jan Mintorovitch, Martin Requardt, and Hanns-Joachim Weinmann. "Comparison of Magnetic Properties of MRI Contrast Media Solutions at Different Magnetic Field Strengths". In: ().

[49] B K Rutt and D H Lee. "The impact of field strength on image quality in MRI." In: *Journal of magnetic resonance imaging : JMRI* 6.1 (1996), pp. 57–62. ISSN: 1053-1807. DOI: 3TLibrary-Converted#12;Usedtobe#1642.

[50] R. Sander. "Compilation of Henry's law constants (version 4.0) for water as solvent". In: *Atmospheric Chemistry and Physics* 15.8 (2015), pp. 4399–4981. ISSN: 16807324. DOI: 10.5194/acp-15-4399-2015.

[51] U Schneider, E. Pedroni, and Antony Lomax. "The calibration of CT Hounsfield units for radiotherapy treatment planning." In: *Physics in medicine and biology* 41.1 (1996), pp. 111–24. ISSN: 0031-9155. DOI: 10.1088/0031-9155/41/1/009. arXiv: arXiv:1011.1669v3. URL: http://www.ncbi.nlm.nih.gov/pubmed/8685250.

[52] *SimpleITK*. \url{http://www.simpleitk.org/}. (Visited on 12/19/2016).

[53] *SimpleITK: IPython Notebooks*. \url{http://insightsoftwareconsortium.github.io/SimpleITK-Notebooks/}. (Visited on 12/19/2016).

[54] *SimpleITK/GettingStarted - KitwarePublic*. \url{https://itk.org/Wiki/SimpleITK/GettingSta. URL: https://itk.org/Wiki/SimpleITK/GettingStarted (visited on 01/10/2017).

[55] A. B. Smith, W. P. Dillon, R. Gould, and Max Wintermark. *Radiation dose-reduction strategies for neuroradiology CT protocols*. 2007. DOI: 10.3174/ajnr.A0814.

[56] Aaron Sodickson, Pieter F Baeyens, Katherine P Andriole, Luciano M Prevedello, Richard D Nawfel, Richard Hanson, and Ramin Khorasani. "Recurrent CT, cumulative radiation exposure, and associated radiation-induced cancer risks from CT of adults." In: *Radiology* 251.1 (2009), pp. 175–184. ISSN: 0033-8419. DOI: 10.1148/radiol.2511081296. URL: http://pubs.rsna.org/doi/abs/10.1148/radiol.2511081296.

[57] Teodor Stanescu, Jans Hans-Sonke, Pavel Stavrev, and B. Gino Fallone. "3T MR-based treatment planning for radiotherapy of brain lesions". In: *Radiology and Oncology* 40.2 (2006), pp. 125–132. ISSN: 13182099. URL: http://www.scopus.com/inward/record.url?eid=2-s2.0-33746661222{\&}partnerID=tZOtx3y1.

[58] Tarraf Torfeh, Rabih Hammoud, Maeve McGarry, Noora Al-Hammadi, and Gregory Perkins. "Development and validation of a novel large field of view phantom and a software module for the quality assurance of geometric distortion in magnetic resonance imaging." In: *Magnetic Resonance Imaging* 33.7 (2015), pp. 939–949. ISSN: 0730725X. DOI: 10.1016/j.mri.2015.04.003. URL: http://eutils.ncbi.nlm.nih.gov/entrez/eutils/elink.fcgi?dbfrom=pubmed{\&}id=25882440{\&}retmode=ref{\&}cmd=prlinks{\%}5Cnpapers3://publication/doi/10.1016/j.mri.2015.04.003http://eutils.ncbi.nlm.nih.gov/entrez/

eutils/elink.fcgi?dbfrom=pubmed{\%}7B{\&}{\%}7Did=25882440{\%}7B{\&
}{\%}7Dretmode=re.

[59] Bernard E. Van Beers, Catherine M. Pastor, and Hero K. Hussain. *Primovist, eovist: What to expect?* 2012. DOI: `10.1016/j.jhep.2012.01.031`.

[60] Hitoshi Wada, Masaki Sekino, Hiroyuki Ohsaki, Tatsuhiro Hisatsune, Hiroo Ike-hira, and Tsukasa Kiyoshi. "Prospect of high-field MRI". In: *IEEE Transactions on Applied Superconductivity*. Vol. 20. 3. 2010, pp. 115–122. ISBN: 1051-8223. DOI: `10.1109/TASC.2010.2043939`.

[61] Amy Walker, Gary Liney, Lois Holloway, Jason Dowling, David Rivest-Henault, and Peter Metcalfe. "Continuous table acquisition MRI for radiotherapy treatment planning: Distortion assessment with a new extended 3D volumetric phantom." In: *Medical physics* 42.4 (2015), p. 1982. ISSN: 0094-2405. DOI: `10.1118/1.4915920`. URL: `http://www.ncbi.nlm.nih.gov/pubmed/25832089`.

[62] Deming Wang, David M. Doddrell, and Gary Cowin. "A novel phantom and method for comprehensive 3-dimensional measurement and correction of geometric distortion in magnetic resonance imaging". In: *Magnetic Resonance Imaging* 22.4 (2004), pp. 529–542. ISSN: 0730725X. DOI: `10.1016/j.mri.2004.01.008`.

[63] Deming Wang, Wendy Strugnell, Gary Cowin, David M. Doddrell, and Richard Slaughter. "Geometric distortion in clinical MRI systems: Part II: Correction using a 3D phantom". In: *Magnetic Resonance Imaging* 22.9 (2004), pp. 1223–1232. ISSN: 0730725X. DOI: `10.1016/j.mri.2004.08.014`.